

See discussions, stats, and author profiles for this publication at: <https://www.researchgate.net/publication/233729261>

nl300140g

DATASET · NOVEMBER 2012

READS

23

8 AUTHORS, INCLUDING:



Carlo Forestiere

University of Naples Federico II

44 PUBLICATIONS 362 CITATIONS

SEE PROFILE



Giovanni Miano

University of Naples Federico II

215 PUBLICATIONS 1,375 CITATIONS

SEE PROFILE



Antonello Tamburrino

Università degli studi di Cassino e del Lazio Me...

128 PUBLICATIONS 706 CITATIONS

SEE PROFILE



Sylvanus Y Lee

Boston University

15 PUBLICATIONS 79 CITATIONS

SEE PROFILE

Genetically Engineered Plasmonic Nanoarrays

Carlo Forestiere,^{†,‡} Alyssa J. Pasquale,[†] Antonio Capretti,^{‡,†} Giovanni Miano,[‡] Antonello Tamburrino,[§] Sylvanus Y. Lee,^{†,||} Björn M. Reinhard,[⊥] and Luca Dal Negro^{*,†}

[†]Department of Electrical and Computer Engineering and Photonics Center, Boston University, 8 Saint Mary's Street, Boston, Massachusetts 02215, United States

[‡]Department of Electrical Engineering, Università degli Studi di Napoli Federico II, via Claudio 21, Napoli, 80125, Italy

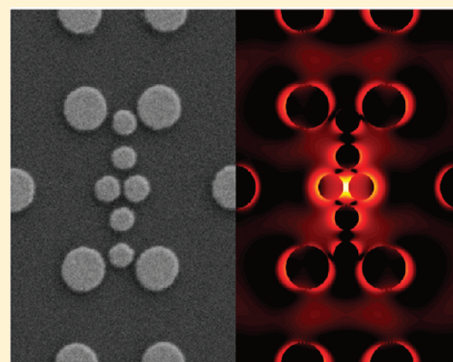
[§]DAIEMI, Università degli Studi di Cassino, Via G. Di Biasio 43, Cassino, 03043, Italy

^{||}Department of Mechanical Engineering, Boston University, 110 Cummington Street, Boston, Massachusetts 02215, United States

[⊥]Department of Chemistry, Boston University, 590 Commonwealth Avenue, Boston, Massachusetts, 02215, United States

S Supporting Information

ABSTRACT: In the present Letter, we demonstrate how the design of metallic nanoparticle arrays with large electric field enhancement can be performed using the basic paradigm of engineering, namely the optimization of a well-defined objective function. Such optimization is carried out by coupling a genetic algorithm with the analytical multiparticle Mie theory. General design criteria for best enhancement of electric fields are obtained, unveiling the fundamental interplay between the near-field plasmonic and radiative photonic coupling. Our optimization approach is experimentally validated by surface-enhanced Raman scattering measurements, which demonstrate how genetically optimized arrays, fabricated using electron beam lithography, lead to order of ten improvement of Raman enhancement over nanoparticle dimer antennas, and order of one hundred improvement over optimal nanoparticle gratings. A rigorous design of nanoparticle arrays with optimal field enhancement is essential to the engineering of numerous nanoscale optical devices such as plasmon-enhanced biosensors, photodetectors, light sources and more efficient nonlinear optical elements for on chip integration.



KEYWORDS: Plasmonics, nanoparticles, nanoantennas, optimization, surface-enhanced Raman scattering, electron-beam lithography

Localized surface plasmons (LSPs) are collective excitations of the free electrons in metal nanostructures coupled to electromagnetic radiation at optical frequencies.¹ The optical excitation of LSPs results in the formation of hot-spots featuring high electric field enhancement over subwavelength spatial regions. Plasmonic devices capable of efficient coupling of electromagnetic radiation to LSP modes in regions with linear dimensions well below the diffraction limit are usually referred to as plasmonic nanoantennas.² Light concentrators based on plasmonic nanoantennas play a key role in many technological applications,³ such as solar cells,⁴ plasmon-enhanced photodetectors,⁵ optical manipulators,⁶ modulators,⁷ thermal emitters,⁸ surface-enhanced Raman scattering substrates,^{9,10} apertureless near-field scanning optical microscopy,¹¹ heat-assisted magnetic recording,¹² and are also ideal to enhance nonlinear optical effects.¹³ Therefore, it is crucial to rationally design reproducible plasmonic nanoparticle arrays (PNAs) capable of producing the highest field enhancement at well-defined locations and targeted frequency spectra for device applications.

Seminal work on the design of metallic nanostructures featuring high-field enhancement relied on self-similar chains of metal nanospheres.¹⁴ Subsequently, more accurate studies¹⁵ including fully retarded electromagnetic interactions demon-

strated large electrical field enhancement in Ag spheres. More recently, Zou and Schatz¹⁶ highlighted the importance of long-range diffractive coupling in nanoparticle (NP) arrays for the enhancement of the electric field intensity in the subwavelength gap of a particle dimer. On the other hand, the use of multiparametric optimization for the design of nanoplasmonic structures has been very limited so far. In particular, recent studies have focused on the optimization of NP shapes and geometrical arrangements for the control of plasmonic resonances¹⁷ and broadband field enhancement,¹⁸ respectively.

The present letter proposes a general procedure for the design of PNAs using a genetic optimization method coupled to a rigorous electromagnetic solver based on analytical multiparticle Mie theory. The proposed approach is not only very effective at selecting the optimal NP arrangements, but it also unveils the most general criteria for the engineering of PNAs. In general, a planar PNA is defined by the NP shape, size, geometrical arrangement, and metal dispersion, which in principle can be considered as optimization degrees of freedom.

Received: January 12, 2012

Revised: February 20, 2012

Published: March 1, 2012

Moreover, in the proposed optimization approach several constraints are enforced to guarantee the physical realizability of the targeted nanostructures within the limitations of the present fabrication techniques, such as requiring a minimum and a maximum allowed NP dimension or a minimum interparticle separation. Several objective functions can in principle be considered, for example, field enhancement value at a given probing point, average field enhancement over a defined spatial region of interest, or scattered power within a prescribed angular cone. In addition, the selected objective function can be maximized for a single frequency (that is, narrow band optimization) or for multiple frequencies (that is, broad band optimization) depending on the particular device application.

Genetic Optimization of Nanoparticles. In this study, we performed an optimization aiming at the design of the best configuration of NPs that yields the best field enhancement at a given wavelength at a single probing point selected in the plane of the array. The chosen objective function responds to the technology requirement of concentrating the electric field in a subwavelength hot spot. The objective function is evaluated through a full wave electromagnetic solver, which has to be chosen with particular care, since the near-field has to be computed efficiently and with high accuracy for the optimization to succeed. Aggregates of spherical particles with different radii can be rigorously treated in the context of the generalized multiparticle Mie (GMM) theory.^{19–21} GMM is an analytic method that extends the single particle Mie theory,²² and it is based on a multipolar expansion of the scattered field in terms of vector spherical wave functions (VSWF), centered on each spherical scatterer. The expansion coefficients for the scattered electromagnetic field are found by enforcing the boundary conditions at each particle surface, and by using the translational addition theorem for VSWF.^{19,20} More informations on the GMM method are provided in the Supporting Information.

The objective function is maximized through an evolutionary algorithm, which is inspired by biological concepts such as natural selection and survival of the fittest. Evolutionary algorithms are among the best suited methods for treating problems with a large number of unknowns, featuring the unique ability of avoiding local maxima, which is the main disadvantage of deterministic algorithms.²³ In particular, the genetic algorithm (GA)²⁴ is very well established in radio-frequency antenna engineering^{25,26} because it can be easily implemented and can naturally benefit from an effective use of parallelism. However this approach has found only limited applications in the field of nano-optics so far.^{17,18} More details on the GA optimization are described in the Supporting Information.

By using the GA, we aim at finding both the spatial arrangement $\{r_1, r_2, \dots, r_N\}$ and the radii $\{R_1, R_2, \dots, R_N\}$ of N spheres that maximize the field enhancement FE_0 at an assigned probing point r_0 . Two different materials, namely Au and Ag, have been investigated using experimentally derived dispersion data.²⁷ The objective function is the field enhancement FE_0 at the probing point r_0 , which is defined by the magnitude of the scattered field divided by the magnitude of the incident field. At each GA iteration the objective function is evaluated several times through the GMM code. We can assume without any loss of generality that r_0 coincides with the origin O of the reference system. The NPs are free to move within predetermined boundaries (either one- or two-dimensional) with constraints

on the edge-to-edge distance δ between any pair of particles, the minimum R_{\min} and maximum R_{\max} NP radius, as well as constraints preventing NPs from overlapping with the probing point r_0 (even if can be in contact with it).

In the next two sections, we apply the proposed method to find the optimal Ag and Au NP one and two-dimensional arrays that maximize FE_0 within the broad search space compatible with the validity of classical electromagnetic theory, namely we only impose $\delta = 3$ nm, $R_{\min} = 5$ nm as lower bounds of our search algorithm. Moreover, $R_{\max} = 150$ nm has been set as an upper bound. The particle arrays are illuminated by linearly polarized plane wave at the plasmonics resonance wavelength, that is, $\lambda^{(Ag)} = 370$ nm for Ag and $\lambda^{(Au)} = 535$ nm for Au, propagating orthogonally to the plane of the array. The corresponding refractive indices, namely $n^{(Ag)}(\lambda^{(Ag)}) = 0.068 - j1.68$ and $n^{(Au)}(\lambda^{(Au)}) = 0.52 - j2.28$, have been obtained from experimental data.²⁷ We then design the optimum NP array for SERS sensing compatible with practical fabrication constraints as a proof of concept device to experimentally validate the optimization approach.

Optimization of Linear Array. Let us first consider the engineering of the radius and the position of an isolated NP whose center is constrained to be on the x axis, which coincides with the polarization direction of the incident plane wave. The GA solution to this initial problem is to position the particle in direct contact with the field point r_0 , while the optimized radius turns out to be $R^{(Au)} = 57$ nm in the case of Au and $R^{(Ag)} = 26.6$ nm for Ag. From a physical standpoint, the optimization process maximizes the coupling of the incoming radiation into the single particle dipolar modes. This goal is achieved by balancing two different needs. On the one hand, in order to minimize high order modes and total losses the particle needs to be small, while on the other hand, because the particle's dipole moment is proportional to its volume, the NP radius should be large enough to maximize the coupling to the electromagnetic radiation. It is worth noticing that the ratio between the optimized radius and the wavelength turns out to be of the same order of magnitude for both materials, which reflects the quasi-static character of the electromagnetic interaction.

Then we apply our GA approach to the optimization of the positions and the radii of NPs linear arrays composed of N particles (N varies from 2 to 6) and excited by a longitudinal polarized plane wave (polarized along the chain axis). The optimized NP positions and radii and the corresponding values of FE_0 are given in Table 1. We find that the optimum solution for $N = 2$ particles for both Au and Ag NPs is a particle dimer composed of NPs with two different radii and an edge-to-edge spacing as small as allowed by the constraint δ , that is, $\delta = 3$ nm. The corresponding hot-spot is located in the gap between

Table 1. NP Abscissae, Radii, and FE_0 Values for Ag and Au Optimized NP Chains

n	Ag			Au		
	x [nm]	R [nm]	FE_0	x [nm]	R [nm]	FE_0
1	36	33	16.2	64	61	4.9
2	−6.5	6.5	248	−29	29	63
3	470	150	301	−491	103	70
4	−431	150	333	511	107	76
5	−215	46	341	1070	99	78
6	250	49	364	−138	45	80

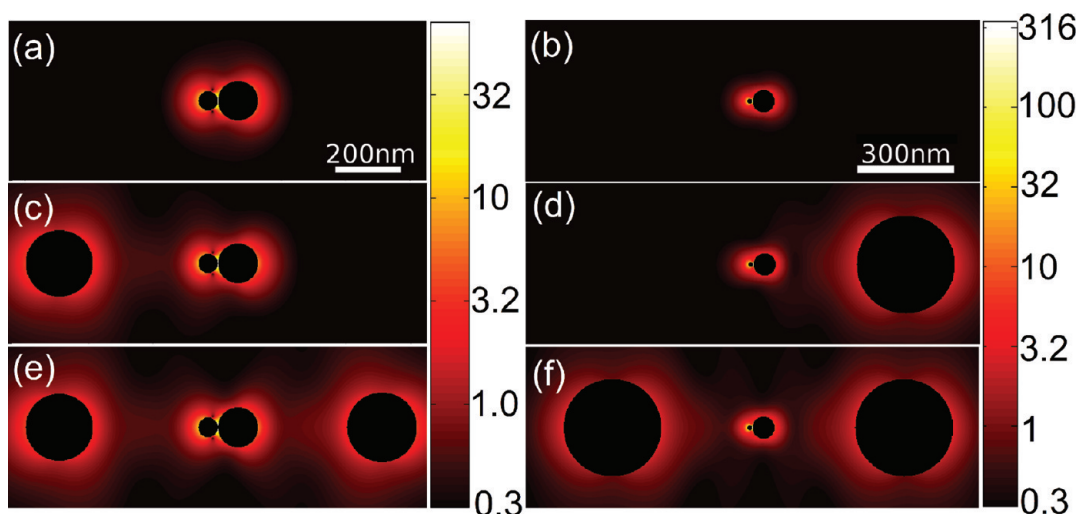


Figure 1. Electric field magnitude on the equatorial plane of the optimized linear 1D arrays composed of (a,b) $N = 2$, (c,d) $N = 3$, and (e,f) $N = 4$ spheres for Au and Ag, respectively. The obtained values of field enhancement at r_0 (r_0 is the center of each simulation box) are (a) 63, (b) 248, (c) 70, (d) 301, 76 (e), and (f) 333. The color maps are in log scale.

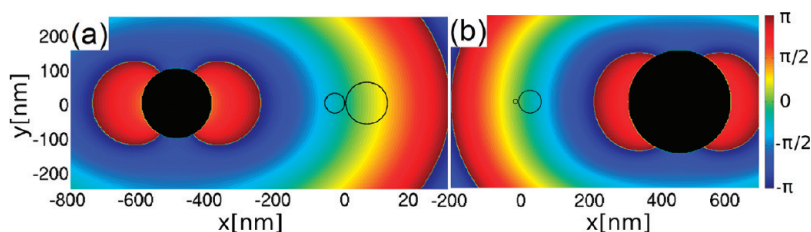


Figure 2. Phase difference between the incident electric field (oriented along the x -axis) and the x -component of the electric field scattered by the 3rd NP in the absence of the first two NPs on the $z = 0$ plane, for gold (a) and silver (b) NPs. The contours of NPs 1 and 2 have been also plotted for convenience. The phase is shown in radian.

the particles, on the surface of the smaller sphere, as shown in Figure 1a for Au and Figure 1b for Ag. Since the Au and Ag dimers feature a strong asymmetry ratio, defined as the ratio of the radii of the two particles, that is, $\rho^{(\text{Au})} = 2.1$, $\rho^{(\text{Ag})} = R_1/R_2 = 5.1$, the local field around the larger NP is only weakly perturbed by the smaller one and the resulting enhancement factor is approximately the product of the enhancement factors of the two isolated NPs.¹⁴

By increasing the number of particles to 3, as shown in Figure 1c for Au and Figure 1d for Ag, the GA solution is to position the center of the third particle at a distance which maximizes the in-phase coupling between the third particle and the dimer at the probing point. The distance between the third particle and the central dimer is selected by the GA in order to produce an in-phase radiative coupling with the external excitation in each particle of the dimer. This is evident in Figure 2, where we plot the calculated phase difference between the incident electric field (oriented along the x -axis) and the x -component of the electric field scattered by the 3rd NP in the absence of the first two NPs on the $z = 0$ plane, for gold (a) and silver (b) NPs. For convenience, we also plot in Figure 2 the contours of NPs 1 and 2. For both Au and Ag particles, we notice that the third NP radiates an electric field whose x -component is in-phase with the external field in the proximity of particles 1 and 2. Therefore, the central dimer experiences a total incident field that is the in-phase superposition of the external field and the field radiated by the third particle. Furthermore, we observe in Figure 1c,d that the third NP in the linear array assumes the maximum allowed radius in order to

maximize the radiative coupling within the limits of inherent material losses. When increasing the NP number to $N = 4$, the GA positions the fourth NP on the opposite side symmetrically with respect to the third to further boost radiative coupling, as is shown in Figure 1e,f for Au and Ag NPs. However, adding further NPs to the linear chain causes a saturation of the field intensity value and additional NPs only contribute with a negligible increase to the field enhancement, as can be seen in Table 1, summarizing the results of the linear chain optimization.

Two-Dimensional Optimization. We now apply the GA to the design of a two-dimensional metal NP array excited by a linearly polarized plane wave propagating orthogonally to the array plane. In order to emphasize the importance of NP arrangement, an optimization was carried out keeping all NP radii constant to $R_0 = 50$ nm, whereas the NP centers were free to move in a 2D box of length $L = 2 \mu\text{m}$ centered at $r_0 = 0$. The optimization results obtained for arrays of NPs with varying size are discussed in the Supporting Information. As shown previously, we found that regardless of the metal choice the $N = 2$ configuration of NPs results in a dimer aligned along the polarization direction with the minimum allowed edge-to-edge spacing. We show this configuration in Figure 3a for Au and panel e for Ag, while the exact particle coordinates are listed in Table 2.

When more particles are added to the system, for instance, when $N = 6$ as shown in Figure 3b, we find that Au NPs assemble to form dimers, placed symmetrically with respect to the probing point along the vertical direction in order to

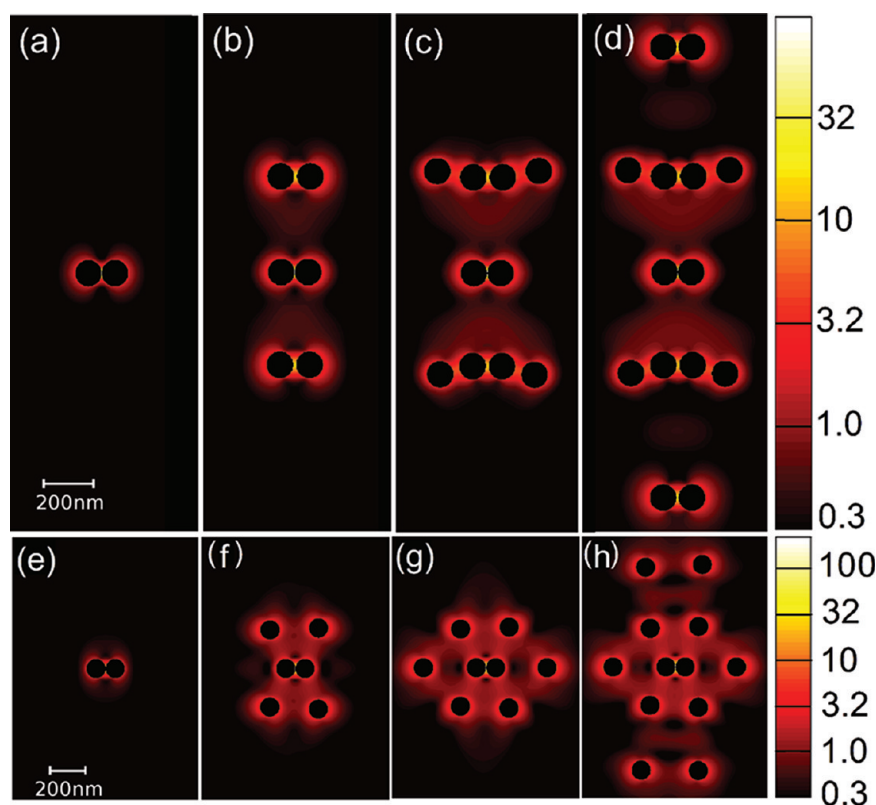


Figure 3. Electric field magnitude on the equatorial plane of 2D optimized arrays composed of (a) $N = 2$, (b) $N = 6$, (c) $N = 10$, and (d) $N = 14$ Au NPs and by (e) $N = 2$, (f) $N = 6$, (g) $N = 8$, and (h) $N = 12$ Ag NPs under horizontal polarization. The obtained values of field enhancement at r_0 (r_0 is the center of each simulation box) are (a) 62, (b) 87, (c) 98, (d) 107, (e) 120, (f) 234, (g) 276, and (h) 306. The color maps are in log scale.

Table 2. NP Coordinates and FE_0 Values of Ag and Au Optimized 2D Arrays with Fixed NP Radius

n	Ag			Au		
	x [nm]	y [nm]	FE_0	x [nm]	y [nm]	FE_0
1	-50	0	120	-50	0	62
2	53	0		53	0	
3	124	-215		-55	-359	
4	-134	-205	234	58	-359	87
5	123	215		-52	370	
6	-133	205		61	370	
7	326	0	276	200	394	98
8	-332	0		-191	393	
9	-180	-550		183	-392	
10	123	-550	306	-180	-390	107
11	-160	540		56	-870	
12	144	540		-56	-870	
13				56	870	
14				-56	870	

provide a radiative contribution in-phase with the external excitation in correspondence of the NPs of the central dimer. The Ag NPs, shown in Figure 3f, contribute similarly but with individual NPs placed along a circumference of radius $R_C = 250$ nm centered at r_0 . This fact is not surprising because two identical electric dipoles, lying on the same circumference, embedded in a homogeneous isotropic medium and excited by the same time-harmonic field, radiate electromagnetic fields with the same phase at r_0 . Moreover, the radius R_C is optimized to achieve an in-phase coupling between the fields radiated by these additional particles and the external excitation at the

central dimer at $\lambda^{(\text{Ag})} = 370$ nm. Furthermore, the particles 3–6 are not randomly placed along this circumference; the lengths of the two chords that have the NP centers as end points (the distances between r_3 and r_4 and between r_5 and r_6 are $d_{3,4} \approx d_{5,6} \approx 257$ nm, respectively) are approximately equal to the radius R_C of the circumferences on which they are positioned. From an electromagnetic standpoint, this means that the GA has maximized not only the far-field radiating contribution of the outer particles to the center, but it has also maximized the in phase coupling among the external particles.

This same phenomenon occurs when we increase N to 10, as shown for Au in Figure 3c and N to 8 for Ag in Figure 3g. In particular, in Figure 3g, the GA aligns the two additional Ag NPs along the axial direction of the dimer made of the first and second NPs, symmetrically with respect to r_0 at distance from the field point $d_{7,0} \approx d_{8,0} \approx 320$ nm.

Finally, by adding further NPs (shown in Figure 3d for Au and Figure 3h for Ag), we find that they are placed further away to maximize the near-field at the probing point *via* in phase second order radiative contributions.

This analysis has demonstrated that the fundamental NP units leading to an optimum radiative coupling turn out to be the isolated particle in the case of Ag aggregates and the NP dimer for Au patterns. This is because the radiative contribution to the localized near field of an isolated Ag NP is much greater than an equivalent size Au NP, and therefore in order to strengthen the radiative contribution Au NPs need to assemble into dimers. In both cases, the distance between the building blocks and r_0 is found to match the external field phase at the central dimer's position for the optimization wavelength.

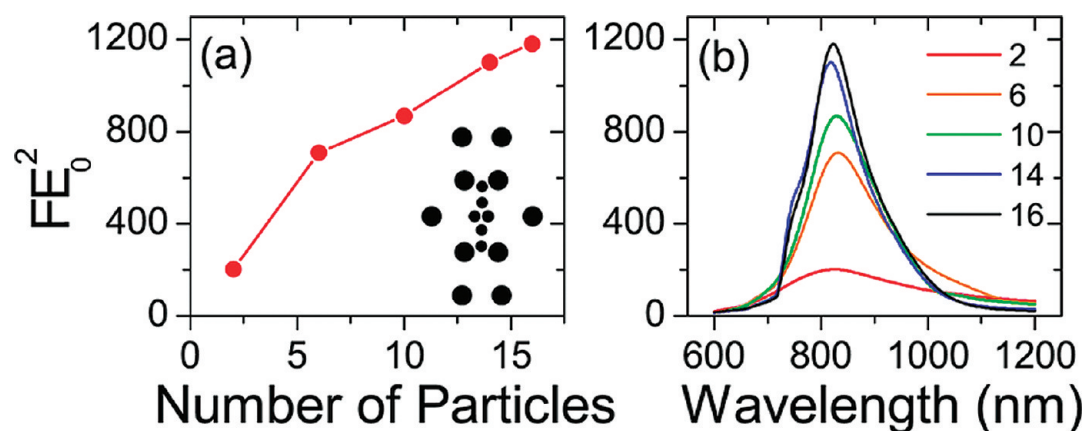


Figure 4. Evolution of the genetic structure as more particles are added to the unit cell. (a) Field enhancement intensity FE_0^2 at the probing point vs the number of particles in the ensemble at the pump wavelength (785 nm). Inset in (a) shows the geometry of the genetic pattern. (b) FE_0^2 spectra of genetic pattern as more particles are added in the optimization.

Experimental Validation. On the basis of the proposed GA method, we design a surface-enhanced Raman scattering (SERS) substrate as a proof of concept device to experimentally demonstrate the feasibility of the proposed optimization approach. Raman scattering is an inelastic light scattering process where incident light interacts with vibrational states of an active object (that is, a molecule, a crystal, etc) causing the scattered light to shift in frequency to lower energy (Stokes-shifted component) and to higher energy (anti-Stokes-shifted component) with respect to the elastic component.²⁸ SERS makes use of enhanced electromagnetic fields on a substrate to vastly increase Raman signals. These enhanced Raman substrates can take the form of random aggregates,¹⁰ periodic gratings,²⁹ dimers,^{30–33} bowties,^{34,35} deterministic aperiodic arrays,^{36,37} or nanoparticle clusters,^{38,39} to name just a few possible geometries. Because the vibrational modes of molecules are unique, SERS is an excellent technique for chemical fingerprinting, and it is a well established and reliable method for label-free chemical and biological sensing.^{9,40} SERS signals have even been detected down to the single molecule limit.⁴¹ Raman enhancements have been shown to scale to the fourth power of local electromagnetic fields, specifically $|E(\lambda_{ex})|^2 |E(\lambda_s)|^2$,³⁰ where λ_{ex} and λ_s are the wavelengths of the pump and Stokes-shifted wavelengths, respectively. For this reason, SERS can be used as an experimental method to determine the near-field properties of devices at these wavelengths.³⁹ Moreover, since the SERS signal is proportional to the number of excited molecules on the substrate and because the electromagnetic field is not uniformly distributed over the substrate, a normalization to the active area is required to obtain a correct estimate of the local field values.

Since the GMM is unable to model a realistic device including arbitrarily shaped particles and an underlying substrate, we used the GA approach discussed above to obtain an initial solution, which was then refined by using a full vector three-dimensional finite-difference time-domain (3D FDTD) simulator. A multiobjective optimization was performed, maximizing the field enhancement for Au NPs at the probing point $r_0 = 0$ for two different wavelengths 785 and 858 nm, which correspond to the laser pump wavelength and Stokes-shifted wavelengths of pMA, respectively.

The NPs were left free to move within a square of edge $L = 2 \mu\text{m}$ with a minimum allowed edge-to-edge distance between any pair of particles $\delta = 25 \text{ nm}$, while the radius of each particle

was forced to be in the interval $[50, 150] \text{ nm}$ for practical fabrication constraints. In the FDTD refinement step, all nanoparticles are assumed to be Au²⁷ nanocylinders with a height of 30 nm, which we have found optimal for near-infrared sensing^{37,36} and are on the top of a glass substrate of refractive index $n = 1.45$.

Using FDTD calculations, we show in Figure 4a the values of the field enhancement intensity FE_0^2 at the probing point r_0 of the genetically optimized structure at the pump wavelength (785 nm) and (panel b) spectra of the FE_0^2 as more particles are added to the simulation window. We can appreciate that the field intensity increases dramatically when N varies from 2 to 6, due to the radiative contribution introduced by the additional particles. As more particles are added to the genetic pattern, the intensity continues to increase but eventually begins to saturate when $N = 14$. The inset in panel a shows the arrangement and size of each nanocylinder in the optimal PNA, while the exact particle coordinates are listed in Table 3. In Figure 4b, we show

Table 3. NP Coordinates and Radii of the Optimized 2D Arrays of Au NPs for SERS

n	x [nm]	y [nm]	R [nm]	n	x [nm]	y [nm]	R [nm]
1	-97	0	72	9	-260	-1000	125
2	75	0	75	10	250	-1000	125
3	-230	460	125	11	0	380	70
4	206	460	125	12	0	175	70
5	-230	-460	125	13	0	-380	70
6	206	-460	125	14	0	-175	70
7	-260	1000	125	15	631	0	125
8	250	1000	125	16	-650	0	125

the spectra of FE_0 and we can see that the wavelength of the near field peak is preserved at the center of the prescribed values of the optimization (the pump and Stokes-shifted wavelengths of pMA) as more particles are added.

These spectra show that by optimizing the focusing of the radiative contribution of large Au nanoparticles into the central dimer we are able to increase the values of near-field enhancement by a factor of 6 with respect to the isolated optimized dimer solution.

Fabrication of Genetically Optimized Arrays. In order to experimentally validate our optimization procedure, we fabricated the genetically optimized array with $N = 16$ and

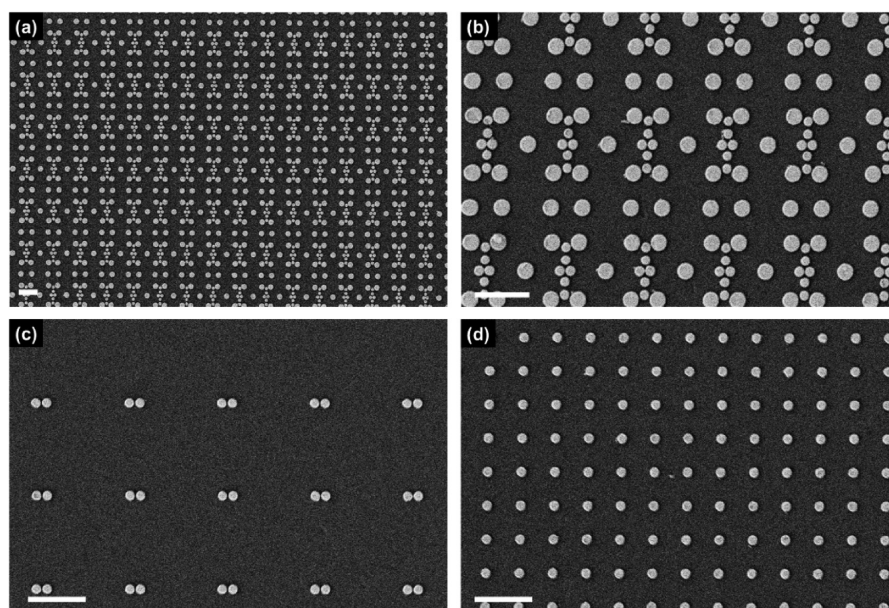


Figure 5. SEM micrographs of SERS substrates. Genetically optimized array (a) and its close-up (b). Dimers (c) (left particle diameter 72.5 nm, right particle diameter 74 nm) spaced 1.5 μm apart. Monomers (d) with 150 nm diameter in a 540 nm lattice. All scale bars correspond to 1 μm .

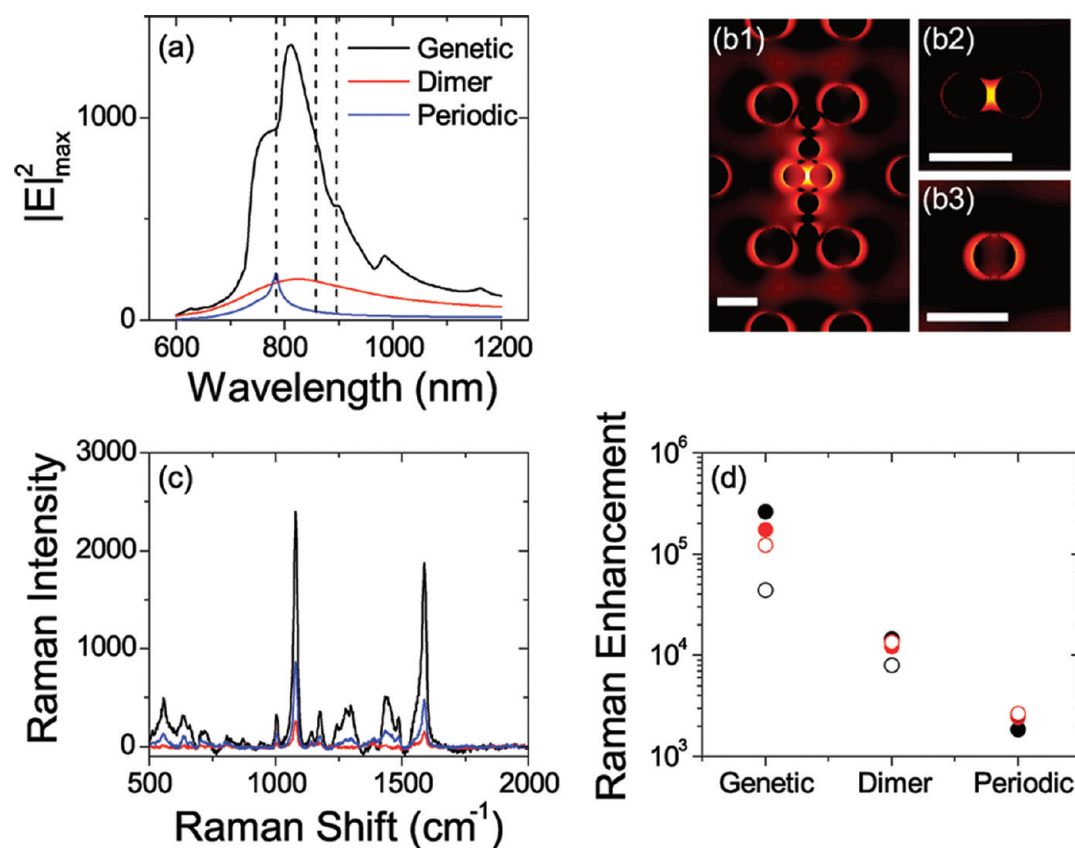


Figure 6. Experimental and theoretical analysis of genetic pattern near-fields. (a) Maximum near-field intensity spectra of the GNA, dimers, and a periodic array optimized at 785 nm. Dashed vertical lines indicate the pump wavelength (785 nm), and two Stokes-shifted wavelengths of interest (1077 and 1590 cm^{-1}). Near-field intensity profiles on the equatorial plane of in logarithmic scale at the pump wavelength of the (b1) GNA, (b2) dimer, and (b3) periodic grating. All scale bars correspond to 300 nm. (c) Measured Raman spectra of the genetic, dimer and periodic patterns and (d) corresponding Raman enhancements for the 1077 cm^{-1} (red) and 1590 cm^{-1} (black) modes of pMA as measured (open circles) and calculated (solid circles).

repeated it in a periodic tiling on the chip. We also fabricated dimers and a periodic grating structure with optimized particle spacing for reference. All these structures exhibit strong

plasmonic resonance in an overlapping spectral region. The periodic tiling was accomplished by stepping-and-repeating the genetic pattern as a base, overlapping the six outer particles. All

of the patterns studied in this paper were fabricated following an electron-beam lithography (EBL) process using a Zeiss SUPRA 40VP SEM equipped with a Raith beam blanker and NPGS nanopatterning software. A 180 nm coating of PMMA 950 (poly(methyl methacrylate)) resist was spun on a quartz substrate and soft baked at 180 °C in an oven for 20 min. In order to eliminate electron-beam charging of the insulating substrate during the lithography process, we make use of a 10 nm sacrificial Au coating. After writing at 30 kV, we develop the samples in MIBK (methyl isobutyl ketone) diluted in isopropanol and deposit 28 nm of Au on top of a 2 nm Ti adhesion layer using electron-beam evaporation. Liftoff was performed by sonicating the samples in acetone.

We show in Figure 5 representative scanning electron micrographs (SEM) of the fabricated arrays. In Figure 5a, we show the genetic nanoarray (GNA) with a close-up of the pattern shown in Figure 5b, confirming the central dimer separation of 25 nm. We also show in Figure 5c dimers with the same diameters as the central dimer of the GNA, spaced 1.5 μm apart to avoid diffractive coupling. Figure 5d shows a periodic array designed to enhance near-fields at 785 nm with a particle diameter of 150 nm and lattice constant of 540 nm. The scale bars all correspond to 1 μm . These SEM micrographs show almost ideal agreement with our design parameters over a large pattern area. Each pattern was spaced by 100 μm to avoid undesired electromagnetic coupling.

SERS Measurements. Turning to a rigorous near-field analysis of genetic, dimer and periodic patterns, we first calculate the maximum near-field intensity supported by each pattern as a function of wavelength when excited with a plane wave polarized along the dimer axis. As seen in Figure 6a, the maximum near-field spectra of the GNA is greatly enhanced over isolated dimers and the periodic arrays. The GNA supports the strongest fields due to the optimal interplay between the near-field coupling at the gap of the central dimer and the radiative contribution of the surrounding particles.

The spatial distributions of the calculated near-field intensity are shown (in logarithmic scale) in Figure 6b1 for the GNA, in Figure 6b2 for individual dimer, and in Figure 6b3 for periodic array at 785 nm, normalized to their maximum field values, with the scale bars corresponding to 300 nm. We see that the genetic patterns exhibit the strongest near-fields in the gap between the two dimer particles, while rather weak near-fields are present around the other particles.

In order to experimentally validate our design procedure we quantified the SERS signal according to the procedure described below.

Following the fabrication process previously discussed, all patterns were plasma ashed in oxygen for 10 min to eliminate any residual PMMA, and then incubated in ethanol with a 10 mM concentration of pMA (p-mercaptoaniline) for 12 h to form a self-assembled monolayer adsorbed on the Au structures. After incubation, the samples were rinsed in pure ethanol before drying with nitrogen. Each pattern was excited by a 785 nm unpolarized diode laser that was fiber coupled to a 40 \times objective (NA = 0.65) through an upright Olympus (BX51 WI) microscope. The laser power focused through the objective was 20.5 mW. The backscattered signal was sent to an electrically cooled (−75 °C) CCD (Andor DU401-BR-DD) via an Andor Shamrock 303i grating spectrometer. The grating used had 600 lines/mm blazed at 750 nm. All spectra were averaged over 10 measurements using a 0.1 s integration time. Prior to taking measurements on any enhanced substrates, the

grating spectrometer was first calibrated by referencing the 520 cm^{-1} line of silicon.

The intensity of the raw Raman signals is shown for comparison in Figure 6c for the GNA, dimers, and periodic array. The genetic pattern shows the strongest Raman signals, while the periodic array has a larger intensity at all Raman modes than the dimers, with the important caveat that there is also more Au present in the periodic structure, which will be corrected for below.

In our analysis, we will consider only the dominant Stokes modes, which are the 1077 and 1590 cm^{-1} modes as shown in panel c of Figure 6.¹⁰ In order to take into account the different amount of Au which contribute to the Raman signal in the different arrays, we calculate Raman enhancement values for each pattern, as previously described in the literature.^{10,42} Unlike periodic and dimer structures, where the field enhancement is uniformly distributed around all the particles within the array, in the case of the genetically optimized pattern only the central dimer contributes to the SERS signal. All other particles in the pattern support very weak electromagnetic fields and would lead to an underestimation of our Raman enhancement. Therefore we have considered only the Au surface area of the central dimer in our calculations of the number of excited pMA molecules for the GNA.

By performing the Raman enhancement calculations on the 1077 (black circles) and 1590 cm^{-1} (red circles) modes on each sample type, we show in Figure 6d the corresponding measured Raman enhancement factors for each geometry (open circles) and a comparison with our FDTD calculations (solid circles). Since unpolarized light was used to experimentally excite the Raman spectrum, in our FDTD calculations of Raman enhancement we considered the enhancement averaged over two orthogonal polarization states. The FDTD calculations predict a logarithmic scaling of enhancement factors for each geometry, which is followed by the experimental data. The GNA exhibits a calculated Raman enhancement of 10^5 , followed by the dimers with 10^4 and the periodic grating with 10^3 enhancement. Experimentally, the periodic structure exhibits an enhancement factor in the low 10^3 range for both modes, which very closely follows our theoretical prediction. The 1077 and 1590 cm^{-1} modes of the dimers were measured to have a Raman enhancement of 7.9×10^3 and 1.3×10^4 . The GNA measured enhancement factors are 4.4×10^4 and 1.2×10^5 for the two Raman modes. All these values are in reasonably good agreement with the FDTD calculations.

The data shown in Figure 6 demonstrate the effectiveness of the GA optimization approach and demonstrate the essential role played by the radiative coupling to enhance near-field strength in the central dimer region of the genetically optimized structures with a large improvement of Raman signals over patterns optimized using conventional dimer or grating geometries.

In this section, we have shown that by genetically optimizing an NP array we can achieve order of ten improvement over NP dimers and order of one hundred improvement over periodic gratings in Raman enhancement. This is essentially accomplished by an optimum interplay between the plasmonic near-field interaction in a NP dimer and the far-field radiative contributions of the surrounding NPs placed at genetically optimized locations.

Conclusions. We have shown that the design of metallic NP clusters for obtaining a very large field enhancement can be performed using the basic paradigm of engineering, namely the

optimization of a well-defined objective function. The investigated scenarios demonstrate that two different mechanisms are at the origin of high field enhancement and need to be simultaneously optimized: the near-field coupling between closely spaced NPs and the far-field radiative coupling of the surrounding NPs. We have unveiled general rules behind the maximization of the radiative coupling. In particular, the building blocks for best electrical field enhancement should be isolated NPs and dimers for Ag and Au aggregates respectively, and the distances between these building blocks should be optimized to obtain constructive interference with the external field excitation at the probing point. Our optimization approach is validated by SERS measurements performed on fabricated devices using pMA monolayers, demonstrating that genetically optimized arrays lead to order of ten improvement over NP dimers, and order of one hundred improvement over periodic gratings in Raman enhancement. A careful design of nano-particle light concentrators can have a large impact in numerous nano-optics applications including solar cells, optical manipulators, plasmon enhanced photodetectors, modulators, and nonlinear optical devices.

■ ASSOCIATED CONTENT

● Supporting Information

Additional information and figures. This material is available free of charge via the Internet at <http://pubs.acs.org>.

■ AUTHOR INFORMATION

Corresponding Author

*E-mail: dalnego@bu.edu.

Notes

The authors declare no competing financial interest.

■ ACKNOWLEDGMENTS

This work was partially supported by the Air Force program “Deterministic Aperiodic Structures for On-chip Nanophotonic and Nanoplasmonic Device Applications” under Award FA9550-10-1-0019, by the NSF Career Award No. ECCS-0846651, and by the project “Engineering structural colors in metal films” sponsored by APIC Corporation and PhotonIC Corporation

■ REFERENCES

- (1) Maier, S. A. *Plasmonics: Fundamental and Applications*; Springer: New York, 2007.
- (2) Novotny, L.; Hecht, B. *Principles of Nano-optics*; Cambridge University Press: New York, 2006.
- (3) Schuller, J. A.; Barnard, E. S.; Cai, W.; Jun, Y. C.; White, J. S.; Brongersma, M. L. *Nat. Mater.* **2010**, *9*, 193–204.
- (4) Atwater, H. A.; Polman, A. *Nat. Mater.* **2010**, *9*, 205–213.
- (5) Tang, L.; Kocabas, S. E.; Latif, S.; Okay, A. K.; Ly-Gagnon, D.; Saraswat, K. C.; Miller, D. A. B. *Nat. Photonics* **2008**, *2*, 226–229.
- (6) Grigorenko, A. N.; Roberts, N. W.; Dickinson, M. R.; Zhan, Y. *Nat. Photonics* **2008**, *2*, 365–370.
- (7) Nikolajsen, T.; Leosson, K.; Bozhevolnyi, S. I. *Appl. Phys. Lett.* **2004**, *85*, 5833–5835.
- (8) Schuller, J. A.; Taubner, T.; Brongersma, M. *Nat. Photonics* **2009**, *3*, 658–661.
- (9) Moskovits, M. *Rev. Mod. Phys.* **1985**, *57*, 783–826.
- (10) Jackson, J. B.; Halas, N. J. *Proc. Natl. Acad. Sci. U.S.A.* **2004**, *101*, 17930–17935.
- (11) Kawata, S.; Inouye, Y.; Verma, P. *Nat. Photonics* **2009**, 388–394.
- (12) Bogy, D. B.; Pan, L. *Nat. Photonics* **2009**, 3.
- (13) Simon, H. J.; Mitchell, D. E.; Watson, J. G. *Phys. Rev. Lett.* **1974**, *33*, 1531–1534.
- (14) Li, K.; Stockman, M. I.; Bergman, D. J. *Phys. Rev. Lett.* **2003**, *91*, 227402.
- (15) Dai, J.; Čajko, F.; Tsukerman, I.; Stockman, M. I. *Phys. Rev. B* **2008**, *77*, 115419.
- (16) Zou, S.; Schatz, G. C. *Chem. Phys. Lett.* **2005**, *403*, 62–67.
- (17) Ginzburg, P.; Berkovitch, N.; Nevet, A.; Shor, I.; Orenstein, M. *Nano Lett.* **2011**, *11*, 2329–2333.
- (18) Forestiere, C.; Donelli, M.; Walsh, G.; Zeni, E.; Miano, G.; Dal Negro, L. *Opt. Lett.* **2010**, *35*, 133–135.
- (19) Bruning, J.; Lo, Y. *IEEE Trans. Antennas Propag.* **1971**, *19*, 378–390.
- (20) Xu, Y. *Appl. Opt.* **1995**, *34*, 4573–4588.
- (21) Gopinath, A.; Boriskina, S.; Feng, N.; Reinhard, B. M.; Dal Negro, L. *Nano Lett.* **2008**, *8*, 2423–2431.
- (22) Bohren, C. F.; Huffman, D. R. *Absorption and Scattering of Light by Small Particles*; Wiley: New York, 1998.
- (23) Chong, E. K. P.; Zak, S. H. *An Introduction to Optimization*; Wiley & Sons: New York, 2001.
- (24) Sivanandam, S.; Deepa, S. *Introduction to Genetic Algorithms*; Springer: New York, 2008.
- (25) Boag, A.; Boag, A.; Michielssen, E.; Mittra, R. *IEEE Trans. Antennas Propag.* **1996**, *44*, 687.
- (26) Haupt, R. *IEEE Antennas Propag. Mag.* **1995**, *37*, 7–15.
- (27) Johnson, P. B.; Christy, R. W. *Phys. Rev. B* **1972**, *6*, 4370–4379.
- (28) Ru, E. L.; Etchegoin, P. *Principles of Surface-Enhanced Raman Spectroscopy: And Related Plasmonic Effects*; Elsevier: New York, 2008.
- (29) Chu, Y.; Banaee, M. G.; Crozier, K. B. *ACS Nano* **2010**, *4*, 2804–2810.
- (30) Banaee, M. G.; Crozier, K. B. *ACS Nano* **2011**, *5*, 307–314.
- (31) Talley, C. E.; Jackson, J. B.; Oubre, C.; Grady, N. K.; Hollars, C. W.; Lane, S. M.; Huser, T. R.; Nordlander, P.; Halas, N. J. *Nano Lett.* **2005**, *5*, 1569–1574.
- (32) Rycenga, M.; Camargo, P. H. C.; Li, W.; Moran, C. H.; Xia, Y. J. *Phys. Chem. Lett.* **2010**, *1*, 696–703.
- (33) Hao, E.; Schatz, G. C. *J. Chem. Phys.* **2004**, *120*, 357–366.
- (34) Fromm, D. P.; Sundaramurthy, A.; Kinkhabwala, A.; Schuck, P. J.; Kino, G. S.; Moerner, W. E. *J. Chem. Phys.* **2006**, *124*, 061101.
- (35) Hatab, N. A.; Hsueh, C.-H.; Gaddis, A. L.; Retterer, S. T.; Li, J.-H.; Eres, G.; Zhang, Z.; Gu, B. *Nano Lett.* **2010**, *10*, 4952–4955.
- (36) Gopinath, A.; Boriskina, S. V.; Reinhard, B. M.; Dal Negro, L. *Opt. Express* **2009**, *17*, 3741–3753.
- (37) Gopinath, A.; Boriskina, S. V.; Premasiri, W. R.; Ziegler, L.; Reinhard, B. M.; Dal Negro, L. *Nano Lett.* **2009**, *9*, 3922–3929.
- (38) Yan, B.; Thubagere, A.; Premasiri, W. R.; Ziegler, L. D.; Dal Negro, L.; Reinhard, B. M. *ACS Nano* **2009**, *3*, 1190–1202.
- (39) Pasquale, A. J.; Reinhard, B. M.; Dal Negro, L. *ACS Nano* **2011**, *5*, 6578–6585.
- (40) Willets, K. A.; Van Duyne, R. P. *Annu. Rev. Phys. Chem.* **2007**, *58*, 267–297.
- (41) Doering, W. E.; Nie, S. J. *Phys. Chem. B* **2002**, *106*, 311–317.
- (42) Zhu, Z.; Zhu, T.; Liu, Z. *Nanotechnology* **2004**, *15*, 357.